

A deep-learning estimate of the decadal trends in the Southern Ocean carbon storage

By Varvara E. Zemskova (barbara.zemskova@utoronto.ca),
Tai-Long He (tailong.he@mail.utoronto.ca),
Zirui Wan,
and
Nicolas Grisouard (nicolas.grisouard@utoronto.ca)

University of Toronto, Department of Physics,
60 St. George Street, Toronto ON M5S 1A7, Canada

This paper is a non-peer reviewed preprint submitted to EarthArXiv.
It was submitted to *Nature Communications* on 12 April, 2021 and is currently undergoing peer review.

Please feel free to reach out to us if you have any questions or comments regarding the paper.

A deep-learning estimate of the decadal trends in the Southern Ocean carbon storage

Varvara E. Zemskova*¹, Tai-Long He^{†1}, Zirui Wan¹, and Nicolas Grisouard¹

¹Department of Physics, University of Toronto, Toronto, ON, Canada

Uptake of atmospheric carbon by the ocean, especially at high latitudes, plays an important role in offsetting anthropogenic emissions^{1,2}. At the surface of the Southern Ocean south of 30°S, the ocean carbon uptake, which had been weakening in 1990s, strengthened in the 2000s^{3,4}. However, sparseness of in-situ measurements in the ocean interior make it difficult to compute changes in carbon storage below the surface^{5,6}. Here we develop a machine-learning model, which estimates concentrations of dissolved inorganic carbon (DIC) in the Southern Ocean up to 4 km depth only using data available at the ocean surface. We applied this model to calculate trends in DIC concentrations over the past three decades and found that DIC decreased in the upper 1 km and increased in deeper layers over this period. However, the particular circulation dynamics that drove these changes may have differed across zonal sectors of the Southern Ocean. While the near-surface decrease in DIC concentrations would enhance atmospheric CO₂ uptake continuing the previously-found trends, weakened connectivity between surface and deep layers and build-up of DIC in deep waters could reduce the ocean's carbon storage potential.

Introduction

Atmospheric CO₂ concentrations have been rising since the pre-industrial era, in large part due to burning of the fossil fuels and land-use changes, such as deforestation and urbanization^{7,8}. Global carbon budget models estimate that oceans absorb about 25% of anthropogenic carbon emissions¹. Polar regions play a particularly important role in carbon uptake, i.e., the transfer of CO₂ from air into the ocean. Indeed, carbon uptake increases with decreasing temperature and increasing wind speed, which enhances mixing at the surface². Consequently, it is estimated that the Southern Ocean is responsible for approximately 40% of the anthropogenic carbon sink⁹, where persistent zonal winds are strong and temperatures are relatively cold.

There has been concern regarding a declining trend in the Southern Ocean carbon uptake from the 1980s into early 2000s^{10,11}. However, recent multidecadal analysis of surface ocean CO₂ measurements found a reversed trend, i.e. that the ocean carbon uptake has been increasing in the 2000s, attributed to changes in ocean circulation, which are primarily due to non-trivial shifts in wind forcing³. However, carbon needs to be exported from the surface down into the ocean interior, where it cannot further exchange with the atmosphere¹². The changes in this export are important not only for the climate but also marine chemistry. An increase in dissolved carbon has led to ocean acidification that subsequently affects marine organisms¹³. However, trends in carbon concentrations in the ocean interior are still poorly understood, primarily for two reasons. First, it is difficult to model biogeochemical cycles in ocean models¹⁴ and second, ocean measurements are spatially and temporally sparse^{5,6}.

To address this sparseness of observations, we developed a neural network model¹⁵ that predicts concentrations of dissolved inorganic carbon (DIC) in the upper 4 km in the ocean using surface and near-surface variables: sea surface temperature, flow velocity at the surface, sea surface height, near-surface wind velocity, surface CO₂ partial pressure ($p\text{CO}_2$). All of the input parameters are readily available via satellite measurements, with the exception of $p\text{CO}_2$, which has been previously estimated by another neural network¹⁶ trained and tested with observational data from Surface Ocean CO₂ Atlas (SOCAT).

We train our model in two phases (see Methods): first us the Biogeochemical Southern Ocean State Estimate (B-SOSE), which is a data assimilating ocean circulation model¹⁴. It is available at a high spatial and temporal resolution of 1/3° and 3-day resolution, respectively, and therefore provides a large volume of data for the initial training. In the second phase, we use DIC measurements from Global Ocean Data Analysis Project version 2 (GLODAPv2) shipboard measurements^{17,18} and Southern Ocean Carbon and Climate Observations and Modeling (SOCCOM) biogeochemical Argo floats¹⁹. These measurements are used to correct any biases originating from the B-SOSE model used in the first phase. Similar to previous works on modeling $p\text{CO}_2$ ²⁰, we find that the model relative error is reduced when using a combination of shipboard and float measurements in the training set.

Observed decadal trends

Using this neural network model, we computed the distribution of five day-averaged DIC concentrations over the 1993 – 2019 period south of 30°S. The depth- and zonally-averaged DIC concentrations (separated into three ocean basins: Atlantic, Pacific, and Indian) are shown in Extended Data Fig. 1 and averaged over three periods (1993-1999, 2000-2009, 2010-2019). Near the surface, DIC concentrations increase polewards with latitude and largely follow the the neutral density surfaces in the interior, consistent with previous estimates²¹. The Pacific and Indian basins, which have older, bottom-sourced waters²² have higher DIC concentrations compared with the Atlantic basin, whose deep waters are ventilated more frequently²².

*barbara.zemskova@utoronto.ca

†tailong.he@mail.utoronto.ca

56 Overall between 1993 and 2019, DIC concentrations have been decreasing near the surface (Figs. 1a-c) and increas-
57 ing in the deep ocean (Figs. 1d-f). The decreasing surface DIC trend, which subsequently lowers $p\text{CO}_2$ at the ocean
58 surface, is consistent with the previously found strengthening of the Southern Ocean carbon sink in the 2000s³. Our
59 analysis shows that this trend continued into the 2010s. However, the changes in DIC concentrations are not zonally
60 uniform, suggesting that distinct mechanisms may exist in different ocean basins (cf. Extended Data Fig. 2).

61 In the 1990s, DIC mostly increased in the upper 1 km over the Pacific within the Antarctic Circumpolar region
62 ($50 - 60^\circ\text{S}$; Figs. 1a, 2d). The predominantly positive phase of the Southern Annular Mode since the 1980s^{23,24} has
63 been associated with the intensification and poleward shift in the Westerlies, the zonally persistent eastward winds at
64 these latitudes. These stronger winds result in flow divergence near the surface and intensify upwelling of DIC-rich
65 waters from the abyss²⁵. Consistent with the signature of stronger upwelling, there is a decrease in DIC in deeper
66 waters (Fig. 1d).

67 While there is also an increasing DIC trend in the South Atlantic and South Indian Oceans in the 1990s along
68 the upwelling isosurfaces at these latitudes (Figs. 1a, 2a,g), the rates are lower than in the South Pacific. The zonal
69 differences could be attributed to the zonal asymmetry in the atmospheric forcing²⁶ that has resulted in greater intensi-
70 fication of the Westerlies over the Pacific than the Atlantic or Indian sectors^{3,27}. The overall increase in DIC is further
71 consistent with the increase in sea surface $p\text{CO}_2$ and increased outgassing or decreased uptake of atmospheric carbon
72 by the Southern Ocean in response to the positive Southern Annular Mode^{10,11,28}. Notably, the strong near-surface
73 negative trend in the Western Indian sector around $40 - 50^\circ\text{S}$ could be because of the increased stratification due to
74 warming in this region over the previous several decades²⁹.

75 In addition to an increase in upwelling, stronger Westerlies in the Southern Hemisphere also lead to an increase in
76 northward Ekman transport³, which at the surface brings sea ice and colder and fresher water from the Antarctic coast.
77 Indeed, decreasing sea surface temperatures^{30,31,32} and increasing freshwater fluxes due to northward sea-ice transport
78 and increased precipitation³³ have been observed over the South Pacific sector starting in the 2000s. To understand the
79 circulation in the Pacific and its role in transport of DIC, we consider effects on water-mass classes of specific neutral
80 density (γ_n) ranges: Circumpolar Deep Water (CDW, $\gamma_n = 27.5 - 28 \text{ kg/m}^3$), Antarctic Intermediate Water (AAIW,
81 $\gamma_n = 27.0 - 27.5 \text{ kg/m}^3$), and Subantarctic Mode Water (SAMW, $\gamma_n = 26.6 - 27.0 \text{ kg/m}^3$)³⁴. CDW comprises of old,
82 dense waters that upwell to the surface south of 55°S ; in South Atlantic, this water-mass is North Atlantic Deep Water
83 (NADW). AAIW comprises of cold and fresh waters that travel northward from the upwelling zone and eventually
84 sink to about 1 km depth, and SAMW of upwelled waters that continue to travel equatorward at the surface before
85 sinking²² (cf. isocontours in Fig. 2).

86 A water-mass can gain buoyancy (become lighter) due to ice melt or lose buoyancy (become denser) due to brine
87 rejection at the surface. In mid- to late-2000s, an increase in melting of advected ice contributed to buoyancy gain
88 of SAMW within the upper 700 m³⁴, which was made even lighter by surface heating north of 40°S ³⁰. Increased
89 freshwater flux from ice melt also has made AAIW lighter, counteracting the buoyancy loss due to cooling at the
90 surface^{34,35}. In contrast, salt fluxes due to brine rejection led to buoyancy loss of CDW, but with large zonal differences.
91 In the Atlantic sector (Weddell Sea), destruction of water-masses in the $27.6 - 27.8 \text{ kg/m}^3$ neutral density range near
92 the surface³⁴ required that water in this density range was upwelled from the interior. However, in the Pacific sector
93 (Ross Sea), positive formation rates of this density range near the surface³⁴ weakened the upwelling.

94 These water-mass transformations can help explain the DIC trends in the Pacific that we find in the 2000s and 2010s.
95 Weakening of CDW upwelling south of 60°S resulted in decreased delivery of old DIC-rich waters to the surface, and
96 hence a weaker increasing trend in DIC near the surface in 2000s (Figs. 1b, 2e). In the 2010s, the near-surface DIC
97 trends further decreased and became negative (Figs. 1c, 2f), while DIC built up (increasing trend) below 1 km depth at
98 the latitudes of CDW upwelling (Figs. 1f, 2f). The decreasing DIC trends follow the AAIW and SAMW density isosur-
99 faces northward, further pointing to weakened upwelling being responsible, as the upwelled CDW comprises a large
100 portion of AAIW and SAMW. Climatologically, these findings are important because a decrease in near-surface DIC
101 concentrations can enhance the uptake of atmospheric carbon by the ocean. However, recent satellite measurements³²
102 found increasing sea surface temperatures over much of the Pacific sector in the 2010s, which may reverse the DIC
103 trends found in this study. While the response of the deeper overturning and upwelling will be delayed, the buoyancy
104 gain of AAIW at surface could stabilize the water column and decrease the export of the DIC from the surface below
105 the mixed layer depth ($\sim 200 - 600\text{m}$ ³⁶) to be sequestered.

106 Unlike the Pacific, most of the Atlantic and Indian sectors of the Southern Ocean, especially between $30 - 60^\circ\text{S}$
107 have been warming and storing heat in the upper 2km over the past few decades^{37,38}. The larger heat uptake over
108 the Southern Ocean compared with the northern temperate and high-latitudes is partially because of the reinforcement
109 of greenhouse gas-induced heating by ozone-hole forcing³⁹ and low levels of aerosols, which could have a cooling
110 effect³⁸, in the Southern Hemisphere. Warming of the upper ocean stabilizes the water column, weakening the effects
111 of the wind-driven upwelling around $50 - 55^\circ\text{S}$. In the Atlantic sector, these changes are reflected in a decrease of a
112 positive trend in DIC concentrations along the upwelling density isosurfaces in 2000s compared with 1990s (Figs. 2a-
113 b). In the upper 1 km, trends are predominantly negative between $45 - 60^\circ\text{S}$ in the 2010s, reflecting the trends of the
114 SAMW/AAIW zonally advected from the Pacific sector (Figs. 1c, 2c). In the Indian sector, we find similar negative
115 trends south of 50°S , but positive trends near the surface to the north (Figs. 1c, 2h,i). The regions of near-surface
116 positive trends correspond to areas, where strong SAMW and AAIW formation rates^{40,41} are enhanced by salinity
117 fluxes⁴² and can help export DIC into the interior (Fig. 2b,c).

118 Furthermore, Atlantic Meridional Overturning Circulation (AMOC) has been weakening since the 1990s^{43,44,45}.
119 AMOC transports dense water sinking in the North Atlantic to the upwelling region in the South Atlantic. The slow-
120 down of AMOC has been attributed to increased uptake of heat by the North Atlantic in response to rising atmospheric
121 greenhouses gas levels⁴³ and weakening of North Atlantic Oscillation since the early 1990s^{38,46}. As a result, meridional
122 transport has weakened and due to buoyancy gain, surface waters in the North Atlantic have been sinking to shallower
123 depths, where DIC content is lower. These changes in the circulation dynamics, which diminish the connectivity be-
124 tween the deep and surface layers, are consistent with our results: progressively decreasing trends along the upwelling
125 density isosurfaces from 1990s to 2010s, especially near the surface, and an increase in DIC concentrations in the inte-
126 rior below 1km depth in the 2010s. Since mid-2010s, increased AMOC transport has been recorded in the subtropics
127 in the Northern Hemisphere^{47,46}. However, because of the long temporal scales in ocean circulation, there will be a

128 lag in response of the Southern Ocean upwelling and DIC concentrations to such changes in the North Atlantic.

129 Discussion

130 Our results show an overall decreasing trend in DIC concentrations in the upper part (top 1 km) of the Southern Ocean
131 over the period from 1993 to 2019. This trend is congruent with the previous findings of decreasing CO₂ uptake in
132 this region in the 1990s and increasing uptake in the 2000s^{3,4}, and indicate the continuation of the increasing uptake
133 potential at the ocean surface into the 2010s. These findings, however, are contrary to an overall increase in DIC
134 concentrations found recently⁶, which computed the decadal changes by comparing the spatially-interpolated data
135 only from biogeochemical floats over the 2014 – 2019 period with shipboard measurements prior to 2005. While
136 floats can augment shipboard data, especially because of superior wintertime coverage, it has been found that models
137 using only data from floats can underestimate the Southern Ocean carbon uptake by threefold compared with models
138 only using shipboard data and by twofold compared with models using a combination of float and shipboard data²⁰.
139 Thus, using only float data in the 2010s could overestimate the DIC concentrations over this time period (subsequently
140 underestimating the carbon uptake at the surface). It would then yield positive long-term DIC trends, contrary to the
141 negative trends found by our model, which integrates data from both shipboard measurements and Argo floats.

142 Our results demonstrate similar effects of weakening upwelling and connectivity between the deep and surface
143 waters in different sectors of the Southern Ocean. Although these trends are in line with the expected changes in
144 ocean circulation, what drives these changes varies zonally. The difference in the underlying mechanisms implies
145 that responses to future changes in the circulation dynamics may also not be zonally uniform. In the current model,
146 we are unable to separate changes in DIC concentrations due to uptake of anthropogenic carbon and due to natural
147 variability in the ocean circulation; it may be pertinent to include methods from previous studies^{5,6} into future analysis.
148 Nevertheless, the decrease in DIC concentrations near the surface that we observe allows for increased uptake of
149 carbon from the atmosphere. However, continued monitoring efforts are necessary to assess the long-term impacts of
150 DIC accumulation on storage of anthropogenic CO₂ in the deep ocean. These changes are important not only from a
151 climatological point of view, but also for the management of marine ecosystems, which are sensitive to acidification⁴⁸.
152 The model presented here can serve as a useful tool for such future studies as it is able to estimate DIC concentrations
153 in the ocean interior up to 4km depth from new satellite measurements as they become available.

154 References

- 155 [1] Corinne Le Quéré et al. “Global carbon budget 2018”. In: *Earth System Science Data* 10.4 (2018), pp. 2141–
156 2194.
- 157 [2] Taro Takahashi et al. “Climatological mean and decadal change in surface ocean pCO₂, and net sea–air CO₂
158 flux over the global oceans”. In: *Deep Sea Research Part II: Topical Studies in Oceanography* 56.8-10 (2009),
159 pp. 554–577.
- 160 [3] Peter Landschützer et al. “The reinvigoration of the Southern Ocean carbon sink”. In: *Science* 349.6253 (2015),
161 pp. 1221–1224.
- 162 [4] Tim DeVries, Mark Holzer, and Francois Primeau. “Recent increase in oceanic carbon uptake driven by weaker
163 upper-ocean overturning”. In: *Nature* 542.7640 (2017), pp. 215–218.
- 164 [5] Nicolas Gruber et al. “The oceanic sink for anthropogenic CO₂ from 1994 to 2007”. In: *Science* 363.6432 (2019),
165 pp. 1193–1199.
- 166 [6] Ben Bronselaer et al. “Importance of wind and meltwater for observed chemical and physical changes in the
167 Southern Ocean”. In: *Nature Geoscience* 13.1 (2020), pp. 35–42.
- 168 [7] Philippe Ciais et al. “Carbon and other biogeochemical cycles”. In: *Climate change 2013: the physical science
169 basis. Contribution of Working Group I to the Fifth Assessment Report of the Intergovernmental Panel on Climate
170 Change*. Cambridge University Press, 2014, pp. 465–570.
- 171 [8] Lucy R Hutyrá et al. “Urbanization and the carbon cycle: Current capabilities and research outlook from the
172 natural sciences perspective”. In: *Earth’s Future* 2.10 (2014), pp. 473–495.
- 173 [9] Tim DeVries. “The oceanic anthropogenic CO₂ sink: Storage, air-sea fluxes, and transports over the industrial
174 era”. In: *Global Biogeochemical Cycles* 28.7 (2014), pp. 631–647.
- 175 [10] Corinne Le Quéré et al. “Response to comments on” Saturation of the Southern Ocean CO₂ sink due to recent
176 climate change”. In: *science* 319.5863 (2008), pp. 570–570.
- 177 [11] Nicole S Lovenduski, Nicolas Gruber, and Scott C Doney. “Toward a mechanistic understanding of the decadal
178 trends in the Southern Ocean carbon sink”. In: *Global Biogeochemical Cycles* 22.3 (2008).
- 179 [12] Dan Jones and Takamitsu Ito. “Gaussian mixture modeling describes the geography of the surface ocean carbon
180 budget.” In: *Proceedings of the 9th International Workshop on Climate Informatics* (2019).
- 181 [13] Katherina Petrou et al. “Acidification diminishes diatom silica production in the Southern Ocean”. In: *Nature
182 Climate Change* 9.10 (2019), pp. 781–786.
- 183 [14] Ariane Verdy and Matthew R Mazloff. “A data assimilating model for estimating Southern Ocean biogeochem-
184 istry”. In: *Journal of Geophysical Research: Oceans* 122.9 (2017), pp. 6968–6988.
- 185 [15] Tai-Long He et al. “Recurrent U-net: Deep learning to predict daily summertime ozone in the United States”.
186 In: *arXiv preprint arXiv:1908.05841* (2019).
- 187 [16] Peter Landschützer et al. “A neural network-based estimate of the seasonal to inter-annual variability of the
188 Atlantic Ocean carbon sink”. In: *Biogeosciences* 10.11 (2013), pp. 7793–7815.
- 189 [17] Are Olsen et al. “GLODAPv2. 2020—the second update of GLODAPv2”. In: *Earth System Science Data Dis-
190 cussions* (2020), pp. 1–41.

- 191 [18] Robert M Key et al. “Global ocean data analysis project, version 2 (GLODAPv2)”. In: *Ornl/Cdiac-162, Ndp-093*
192 (2015).
- 193 [19] Kenneth S. Johnson et al. “Southern Ocean Carbon and Climate Observations and Modeling (SOCCOM) Float
194 Data Archive”. In: (2019). URL: <https://doi.org/10.6075/J01G0JKT>.
- 195 [20] Seth M Bushinsky et al. “Reassessing Southern Ocean air-sea CO₂ flux estimates with the addition of biogeo-
196 chemical float observations”. In: *Global biogeochemical cycles* 33.11 (2019), pp. 1370–1388.
- 197 [21] Yingxu Wu et al. “What drives the latitudinal gradient in open-ocean surface dissolved inorganic carbon con-
198 centration?” In: *Biogeosciences* 16.13 (2019), pp. 2661–2681.
- 199 [22] Lynne D Talley. “Closure of the global overturning circulation through the Indian, Pacific, and Southern Oceans:
200 Schematics and transports”. In: *Oceanography* 26.1 (2013), pp. 80–97.
- 201 [23] Gareth J Marshall et al. “Causes of exceptional atmospheric circulation changes in the Southern Hemisphere”.
202 In: *Geophysical Research Letters* 31.14 (2004).
- 203 [24] Alexander Sen Gupta and Matthew H England. “Coupled ocean–atmosphere–ice response to variations in the
204 southern annular mode”. In: *Journal of Climate* 19.18 (2006), pp. 4457–4486.
- 205 [25] Darryn W Waugh et al. “Recent changes in the ventilation of the southern oceans”. In: *Science* 339.6119 (2013),
206 pp. 568–570.
- 207 [26] Marilyn N Raphael et al. “The Amundsen Sea low: Variability, change, and impact on Antarctic climate”. In:
208 *Bulletin of the American Meteorological Society* 97.1 (2016), pp. 111–121.
- 209 [27] Andrea F Carril and Antonio Navarra. “Low-frequency variability of the Antarctic Circumpolar Wave”. In:
210 *Geophysical Research Letters* 28.24 (2001), pp. 4623–4626.
- 211 [28] Carolina O Dufour et al. “Eddy compensation and controls of the enhanced sea-to-air CO₂ flux during positive
212 phases of the Southern Annular Mode”. In: *Global Biogeochemical Cycles* 27.3 (2013), pp. 950–961.
- 213 [29] Friedrich A Schott, Shang-Ping Xie, and Julian P McCreary Jr. “Indian Ocean circulation and climate variabil-
214 ity”. In: *Reviews of Geophysics* 47.1 (2009).
- 215 [30] Dean Roemmich et al. “Unabated planetary warming and its ocean structure since 2006”. In: *Nature climate*
216 *change* 5.3 (2015), pp. 240–245.
- 217 [31] Yavor Kostov et al. “Contributions of greenhouse gas forcing and the Southern Annular Mode to historical
218 Southern Ocean surface temperature trends”. In: *Geophysical Research Letters* 45.2 (2018), pp. 1086–1097.
- 219 [32] Claire E Bulgin, Christopher J Merchant, and David Ferreira. “Tendencies, variability and persistence of sea
220 surface temperature anomalies”. In: *Scientific reports* 10.1 (2020), pp. 1–13.
- 221 [33] F Alexander Haumann et al. “Sea-ice transport driving Southern Ocean salinity and its recent trends”. In: *Nature*
222 537.7618 (2016), pp. 89–92.
- 223 [34] Ryan P Abernathy et al. “Water-mass transformation by sea ice in the upper branch of the Southern Ocean
224 overturning”. In: *Nature Geoscience* 9.8 (2016), pp. 596–601.
- 225 [35] Ivana Cerovečki et al. “The effects of enhanced sea ice export from the Ross Sea on recent cooling and freshening
226 of the southeast Pacific”. In: *Journal of Climate* 32.7 (2019), pp. 2013–2035.
- 227 [36] B Buongiorno Nardelli et al. “Southern Ocean mixed-layer seasonal and interannual variations from combined
228 satellite and in situ data”. In: *Journal of Geophysical Research: Oceans* 122.12 (2017), pp. 10042–10060.
- 229 [37] Thomas L Frölicher et al. “Dominance of the Southern Ocean in anthropogenic carbon and heat uptake in CMIP5
230 models”. In: *Journal of Climate* 28.2 (2015), pp. 862–886.
- 231 [38] Jia-Rui Shi, Shang-Ping Xie, and Lynne D Talley. “Evolving relative importance of the Southern Ocean and
232 North Atlantic in anthropogenic ocean heat uptake”. In: *Journal of Climate* 31.18 (2018), pp. 7459–7479.
- 233 [39] David Ferreira et al. “Antarctic Ocean and sea ice response to ozone depletion: A two-time-scale problem”. In:
234 *Journal of Climate* 28.3 (2015), pp. 1206–1226.
- 235 [40] Ivana Cerovečki and Matthew R Mazloff. “The spatiotemporal structure of diabatic processes governing the
236 evolution of Subantarctic Mode Water in the Southern Ocean”. In: *Journal of Physical Oceanography* 46.2
237 (2016), pp. 683–710.
- 238 [41] Libao Gao, Stephen R Rintoul, and Weidong Yu. “Recent wind-driven change in Subantarctic Mode Water and
239 its impact on ocean heat storage”. In: *Nature Climate Change* 8.1 (2018), pp. 58–63.
- 240 [42] Nikolaos Skliris et al. “Salinity changes in the World Ocean since 1950 in relation to changing surface freshwater
241 fluxes”. In: *Climate dynamics* 43.3-4 (2014), pp. 709–736.
- 242 [43] Martha W Buckley and John Marshall. “Observations, inferences, and mechanisms of the Atlantic Meridional
243 Overturning Circulation: A review”. In: *Reviews of Geophysics* 54.1 (2016), pp. 5–63.
- 244 [44] Eleanor Frajka-Williams et al. “Atlantic meridional overturning circulation: Observed transport and variability”.
245 In: *Frontiers in Marine Science* 6 (2019), p. 260.
- 246 [45] Levke Caesar et al. “Current Atlantic Meridional Overturning Circulation weakest in last millennium”. In: *Nature*
247 *Geoscience* (2021), pp. 1–3.
- 248 [46] Ben I Moat et al. “Pending recovery in the strength of the meridional overturning circulation at 26° N”. In:
249 *Ocean Science* 16.4 (2020), pp. 863–874.
- 250 [47] E Frajka-Williams et al. “Coherent circulation changes in the Deep North Atlantic from 16 N and 26 N transport
251 arrays”. In: *Journal of Geophysical Research: Oceans* 123.5 (2018), pp. 3427–3443.
- 252 [48] Scott C Doney et al. “Ocean acidification: the other CO₂ problem”. In: *Annual review of marine science* 1
253 (2009), pp. 169–192.

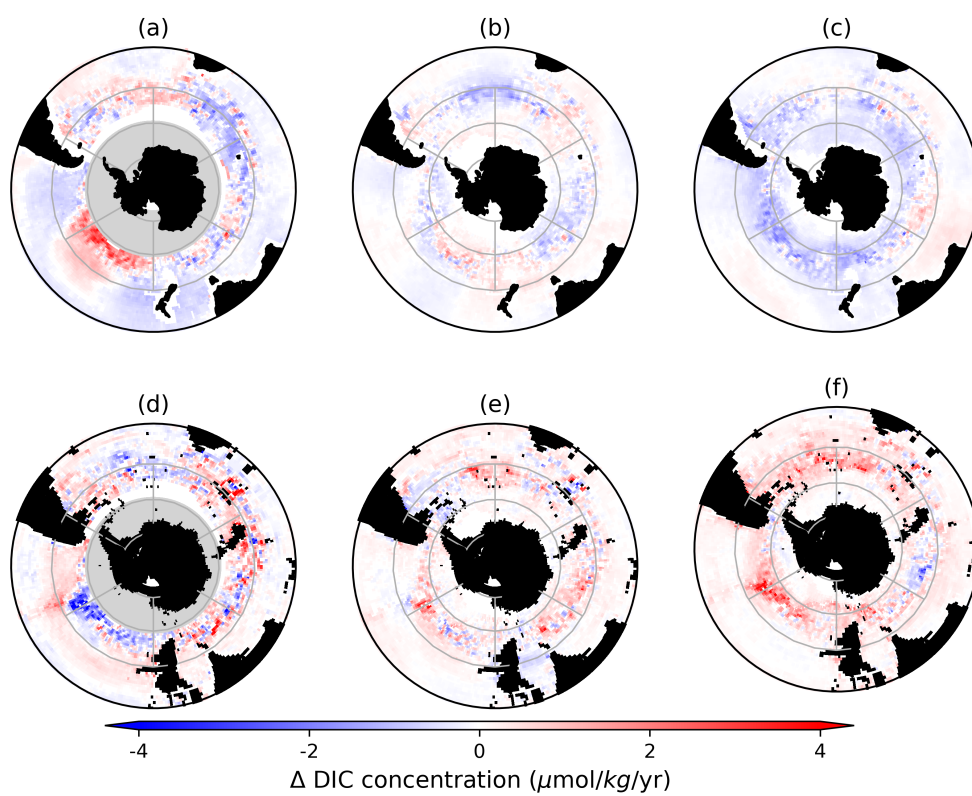


Figure 1: **Linear trends in DIC concentration.** (a-c) averaged over top 1 km, (d-f) averaged over 2 – 4 km depth. Values are calculated over: (left) 1993-1999, (middle) 2000-2009, and (right) 2010-2019. Linear trends outside the 5% significance level ($p \geq 0.05$) are excluded. Areas shaded in grey indicate regions of insufficient data for trend calculations.

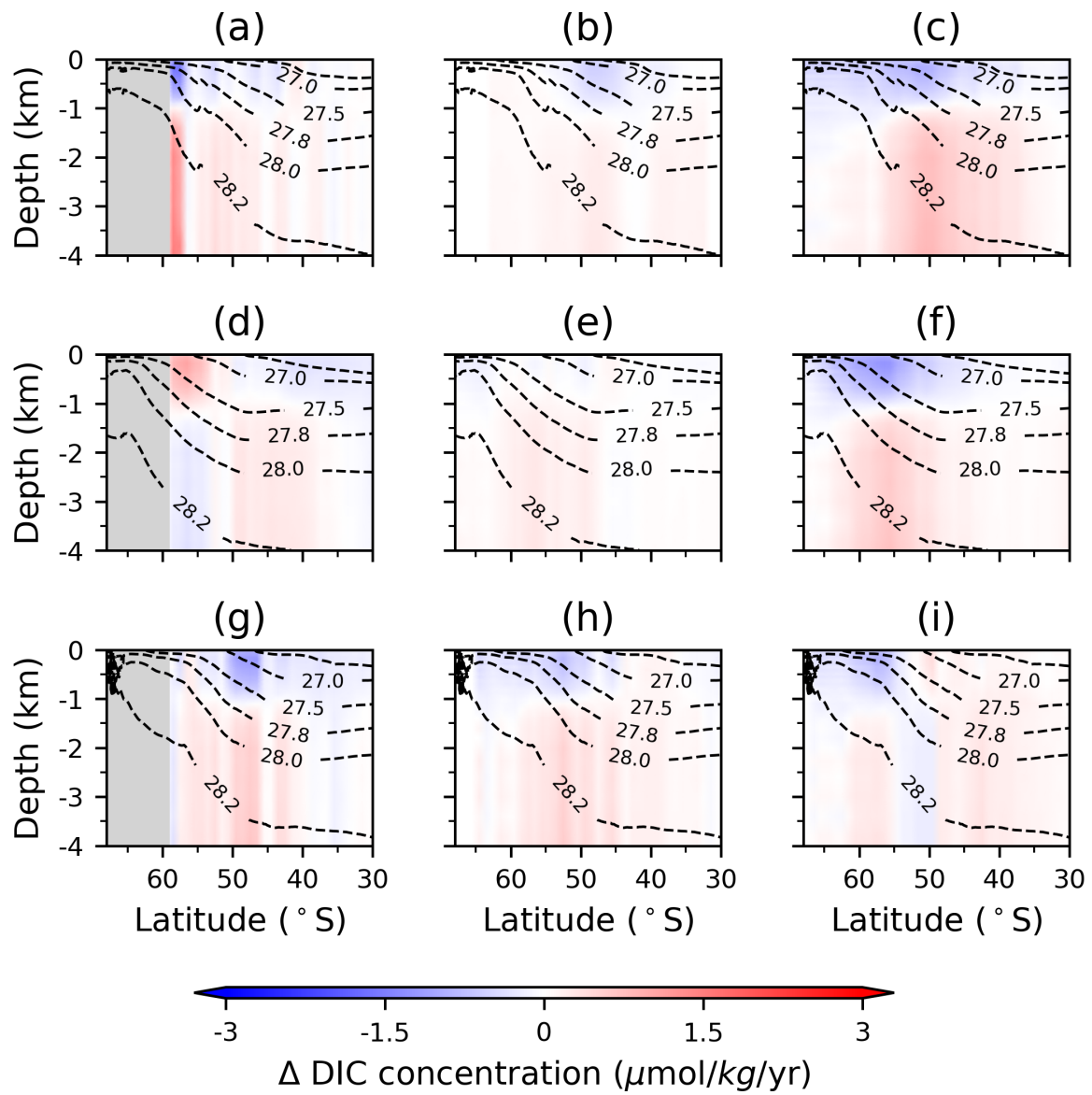


Figure 2: **Linear trends in DIC concentration with depth: (left) 1993-1999, (middle) 2000-2009, (right) 2010-2019.** Zonal means of (a-c) Atlantic, (d-e) Pacific, and (g-i) Indian Oceans. Black dashed contours correspond to isosurfaces of neutral density γ_N from B-SOSE averaged zonally and temporally over 2008-2012 (unlabeled contour: $\gamma_N = 26.6 \text{ kg/m}^3$).

254 Methods

255 Deep-learning model

256 The deep-learning model, which is a type of a neural network, used in this study was adapted from the Recurrent U-net
257 introduced in a previous study aimed to predict atmospheric ozone concentrations¹⁵. The schematic diagram of the
258 model is shown in Figure 3. The model consists of both convolutional neural networks (CNNs) and recurrent neural
259 networks (RNNs)⁴⁹. The first 3 convolutional blocks are used as an encoder, which transforms the input information
260 into high-dimensional feature space using trainable parameters. Trainable parameters in each convolutional block in-
261 clude the weights and biases in the fully-connected layers⁵⁰ and the convolutional kernels in the convolutional layers.
262 The output from the 3rd convolutional block is then forwarded into a long short-term memory⁵¹ (LSTM) cell to capture
263 temporal dynamics in the features. After the LSTM cell, the relationship between these features and the output vari-
264 ables is captured by a decoder, which contains another 3 convolutional blocks with descending depths. Three residual
265 learning connections are added between the encoder and the decoder parts, in order to stabilize the training and capture
266 more direct relationship between input and output variables⁵². We used the mean squared error loss function to train
267 the deep-learning model on a NVIDIA T4 Tensor graphics processing unit (GPU). The Adam optimization algorithm
268 was applied to boost the speed of training⁵³.

269 In this model, we used sea surface temperature, sea surface height, ocean surface velocities, 10 m wind speeds,
270 total heat flux at the ocean surface, ocean surface chlorophyll-a, and ocean surface partial pressure of CO₂ as input
271 variables (predictors). The developed model predicts dissolved inorganic carbon (DIC) concentrations south of 30°S in
272 the upper 4 km of the ocean. These input variables attempted to capture physical (e.g., ocean circulation and mixing),
273 biological (e.g., uptake of CO₂ by photosynthetic organisms), and chemical (e.g., uptake of atmospheric CO₂ at ocean
274 surface) processes that may affect DIC distribution. While there are many other factors (e.g. sinking rates of organic
275 matter, organic matter remineralization rates, total alkalinity, calcification) that could change DIC concentrations, we
276 chose variables that could be easily measured at the ocean surface, such that the measurements better constrained and
277 available at higher spatial and temporal resolutions than measurements in the ocean interior. We trained the deep-
278 learning model in two phases: first augmenting the volume of data using a biogeochemical ocean circulation model,
279 and then correcting for biases of this model using observational data. We detail the datasets that we used and each of
280 the training phases in the following sections.

281 Ocean carbon sink has been previously estimated using different methods. However, these methods may either
282 produce indirect bulk estimates over an entire ocean basin (i.e., inverse models⁵⁴), be numerically expensive (i.e.
283 ocean circulation models¹⁴), or have limited temporal coverage (i.e., interpolations of direct measurements^{5,6}). Our
284 deep-learning model attempted to address these issues. In our model, because of the high spatio-temporal availability
285 of the satellite-based input variables, we were able to create a dataset of DIC concentrations at 1° horizontal resolution
286 in the upper 4 km of the ocean at 5-day intervals between 1993 – 2019. It allowed us to create a timeseries and
287 compute DIC trends at each individual grid cell over this time period. As a result, we were able to explore spatial
288 patterns in temporal trends, rather than only comparing aggregate decadal averages as in previous studies^{5,6}. Using
289 neural networks is also advantageous, as they can capture non-linear relationships between the predictor variables, in
290 contrast to the linear regression models used in previous studies⁵. In addition, this deep-learning model can compute
291 DIC concentrations over the entire Southern Ocean domain very quickly (order of 1 – 2 T4 GPU computational hours
292 required for one year of DIC calculations), which makes it ideal for future monitoring of the ocean carbon sink using
293 new satellite data as it becomes available. Finally, it is important to note that a previous study²⁰ showed that errors of
294 neural network predictions are reduced when the domain is constrained to a single basin rather than the global ocean,
295 and our model was developed and trained specifically over the Southern Ocean basin only.

296 Data sets

297 Biogeochemical Southern Ocean State Estimate (B-SOSE)

298 B-SOSE¹⁴ is a data-assimilating model that incorporates Biogeochemistry with Light, Iron, Nutrients, and Gases model
299 (BLING)⁵⁵ into a data-constrained general circulation model of the Southern Ocean (SOSE)⁵⁶. The model has uniform
300 horizontal resolution of 1/3° over 30 – 78°S; spacing of 52 vertical layers varies with depth from 4.2 m near the
301 surface to 400 m in the deepest layers. The output data contains both physical (e.g., temperature, salinity, flow velocity)
302 and biogeochemical (e.g., concentrations of DIC, dissolved oxygen, pH, and chlorophyll-a). It is available at 3-day
303 intervals over 2008 – 2012 period. The biogeochemical portion of the model includes carbon, nitrogen, and phosphorus
304 cycling, phytoplankton population dynamics, and iron chemistry. The model assimilates in-situ observational data of
305 the carbon system, oxygen, and nutrients from bgc-Argo, GLODAPv2¹⁷, and Surface Ocean CO₂ product version 4
306 (SOCATv4)⁵⁷ in addition to physical constraints from hydrographic and satellite observations.

307 Satellite-based products

308 We used data from the following sets produced based on satellite observations. All data was available over between
309 1993 – 2019 over the Southern Ocean (i.e. south of 30°S), with the exception of chl-a, which was only available north
310 of 60°S.

- 311 • Horizontal ocean surface velocities (u, v) were obtained from Ocean Surface Current Analysis Real-time (OS-
312 CAR)^a, which uses satellite sea surface height, wind, and temperature for computations⁵⁸. Data are available at
313 1/3° and 5-day resolution between 1992 – 2020.
- 314 • Sea surface height (SSH) was obtained from Copernicus Marine Environment Monitoring Service (CMEMS)
315 dataset^b that merges altimetry data from available missions for a more consistent and homogeneous product. It

^ahttps://podaac.jpl.nasa.gov/dataset/OSCAR_L4_OC_third-deg

^bhttps://resources.marine.copernicus.eu/,dataset:SEALEVEL_GLO_PHY_L4_REP_OBSERVATIONS_008_047

316 is available $1/4^\circ$ and 5-day resolution between 1993 – 2020. SSH was used to compute vertical velocity (w)
317 at the ocean surface to be consistent with calculations in B-SOSE.

- 318 • Zonal and meridional components of 10 m wind speed, sea surface temperature (SST), and total heat flux at the
319 ocean surface were obtained from ERA5⁵⁹, which is a comprehensive reanalysis dataset that assimilates available
320 observations in the upper air and near surface. Data^c is available at an hourly temporal resolution and 31 km
321 spatial resolution from 1979 – 2020. Total heat flux was computed as the sum of net shortwave and longwave
322 radiation and sensible and latent heat, using the hourly accumulation values (in J/m^2) converted to flux units
323 (W/m^2).
- 324 • Surface chlorophyll-a (chl-a) concentrations were obtained from GlobColour dataset^d by the European Space
325 Agency, which merges data from four satellite sources. Data used here is available at $1/4^\circ$ and 8-day resolution
326 from 1997 – 2020.
- 327 • An estimate from neural network¹⁶ was used for surface partial pressure of CO_2 (pCO_2). This neural network
328 uses primarily satellite observations as inputs to interpolate the available shipboard measurements of pCO_2 over
329 1° grid at a monthly resolution from 1982 – 2020. Using this neural network-based dataset is advantageous
330 compared to simply spatially-interpolated observations because it accounts for spatial and temporal heterogeneity
331 of observational data availability.

332 Observational DIC data

333 We trained the model with DIC data from two observational datasets. The first one was GLObal Ocean Data Analysis
334 Project Version 2 (GLODAPv2)^{17,18}, which is a compilation of inorganic carbon data collected during research cruises.
335 We used in-situ data from the original shipboard measurements rather than a globally remapped product. The second
336 dataset was collected by Southern Ocean Carbon and Climate Observations and Modeling project (SOCCOM)^e Argo
337 floats equipped with biogeochemical sensors. Here we only use data with “good” quality flag. We used GLODAPv2
338 shipboard measurements available between 1998 – 2019 and Argo float measurements available between 2014 –
339 2019. Over the period where the two datasets overlap, the number of Argo float measurements was much larger
340 than that of the shipboard measurements (cf. Extended Data Fig. 4). Argo float data also had better temporal coverage,
341 whereas wintertime shipboard measurements were limited²⁰. However, data from Argo floats was only available above
342 2 km depth, whereas there were shipboard measurements below this depth, though far less numerous than above (cf.
343 Extended Data Fig. 4). Furthermore, it has been shown using both Argo float and shipboard measurements in neural
344 network training minimizes the root mean square error between the model predictions and observations²⁰, so we used
345 both datasets for training our model.

346 Model training

347 The high spatial and temporal resolutions of B-SOSE over a three-dimensional domain made it a good training set for
348 a deep-learning model. B-SOSE data was also more evenly distributed spatially and temporally than the observations.
349 In particular, it had significantly more data points available below 2 km, where observations were especially sparse.
350 Thus, including B-SOSE dataset into training was important to prevent overfitting of the deep-learning model to the
351 observational data. To correct for any inherent errors of the B-SOSE model and to account for its short availability
352 period (only 5 years), it was also necessary to further train a model with observed data (i.e. shipboard and Argo float
353 measurements). However, because of the vast difference in the number of available data points between B-SOSE
354 (~ 10 million data points per timestep over 609 timesteps) and observations ($\sim 450,000$ data points in total), it was
355 necessary to train the model in two phases; otherwise, the deep-learning model output would have been heavily biased
356 towards B-SOSE. Finally, because the near-coastal processes in shallow waters may be significantly different from the
357 dynamics of the open ocean, we excluded regions with less than 1 km depth from our model training.

358 Phase 1

359 In the first training phase of the deep-learning model, we used SSH, ocean surface velocities (u, v, w), ocean surface
360 heat flux, pCO_2 , and chl-a concentrations from B-SOSE output and SST and 10 m wind speed velocities from ERA5.
361 We chose to use these two predictors from ERA5 rather than B-SOSE output because of the higher spatio-temporal
362 resolution of the ERA5 data, which would be advantageous for matching to the in-situ measurements in Phase 2 of
363 the model training. The hourly ERA5 data was averaged over 3-day period to have the same temporal resolution as
364 B-SOSE. DIC concentrations from B-SOSE were taken as the target for model training. We used data over 2008 – 2011
365 period for model training, while reserving a randomly-sampled 10% of it for in-sample validation to prevent overfitting.
366 The 2012 data was then used as out-of-sample validation set for the model.

367 The comparison with model-predicted DIC from Phase 1 training and B-SOSE DIC are shown in Extended Data
368 Fig. 5, averaged over 1 km depth intervals over the year 2012, which we chose as the testing period for the model. The
369 relative errors were overall less than $\pm 5\%$ within each depth interval; the errors did, however, increase with depth,
370 where fewer data points were available because of the larger vertical grid spacing and the range of DIC concentration
371 values was not as large compared to the surface. In the deep layers (below 2 km depth), the model overestimated DIC
372 concentrations in the Atlantic sector and underestimated them in the Pacific sector north of $45^\circ S$ with relative errors
373 much larger than in the poleward regions. Northward of these latitudes, exchange with other ocean basins plays an
374 important role in the deep circulation, and it is possible that local surface and near-surface properties were not sufficient
375 to capture the inter-basin transport dynamics²⁰. As such, we were careful in not discussing DIC trends in this part of
376 the ocean in text.

^c<https://cds.climate.copernicus.eu/cdsapp#!/home>

^dhttps://www.globcolour.info/products_description.html

^e<https://soccom.princeton.edu/>

377 The relative errors were centered and symmetrically distributed around approximately zero at all depths (cf. Ex-
378 tended Data Fig. 6). The errors showed overall no systematic bias towards high or low values, though there were more
379 high-end outliers compared with low-end outliers below 2 km. The spread (including the outliers) was larger in the up-
380 per 1 km, possibly related to a greater degree of noise associated with small-scale near-surface processes that was more
381 difficult to capture with the model. Horizontally-averaged profile of model-predicted DIC concentration also showed
382 very small deviation (less than 0.2% from B-SOSE data across different depth levels (cf. Extended Data Fig. 7)).

383 The heatscatter plot of DIC concentrations predicted by the deep-learning model over the three-dimensional domain
384 for 2012 is shown in Extended Data Fig. 8 in comparison with B-SOSE DIC concentrations. The vast majority of the
385 points were along the one-to-one line with a high linear correlation coefficient ($r^2 = 0.98$) between the model-predicted
386 and B-SOSE DIC concentrations. The offset of the linear correlation was also small ($45 \mu\text{mol}/\text{kg}$), especially given
387 that DIC concentrations were mostly within the $2050 - 2350 \mu\text{mol}/\text{kg}$ range.

388 Phase 2

389 In the second training phase, we applied the deep-learning model obtained from Phase 1 to the previously-described
390 satellite-based observational data and further trained the model to minimize the RMSE between the model predictions
391 and shipboard and Argo float measurements. When chl-a measurements were not available (primarily due to presence
392 of sea ice), values within those cells were set to zero to be consistent with B-SOSE instead of setting it to a non-zero
393 minimum chl-a concentration value like in some previous $p\text{CO}_2$ models⁶⁰. The observational DIC data was re-mapped
394 to the same depth levels as the B-SOSE dataset to be consistent with Phase 1 training output. We used the most recent
395 20% of the observational data as an out-of-sample test dataset, and the rest as the training dataset. Again, a randomly-
396 sampled 10% of the training set was used for in-sample testing. To compare the two observational DIC datasets, we
397 trained the model with (1) only shipboard data, and (2) with shipboard and Argo float data.

398 The distributions of relative errors of the model prediction (cf. Extended Data Fig. 9) were again mostly symmetric
399 around zero with most values falling between $\pm 3\%$. The outliers could be the result of both model prediction errors
400 and the variability in data collection from different cruises and any systematic differences between shipboard and Argo
401 float measurements. As expected, the correlation between predicted and observed DIC concentration values improved
402 when the model is trained with more data points by including the Argo float measurements (compare Extended Data
403 Fig. 10a,b). When the model was trained with both shipboard and Argo float data, considerably more model-predicted
404 points fell along the one-to-one line. This result is consistent with previous analysis of neural networks used for to com-
405 pute $p\text{CO}_2$, concluding that both shipboard and Argo float data were necessary for more accurate model predictions²⁰.
406 However, because of the much more limited number of observations compared with the number of available B-SOSE
407 data points, the linear fit (e.g., correlation coefficient) was worse compared with Phase 1 training (cf. Extended Data
408 Fig. 8). This demonstrated that performance of a deep-learning model improved with more data points available for
409 training and why it was important to pre-train the model with a large volume of B-SOSE data in Phase 1.

410 Linear decadal trend estimations

411 We applied the trained deep-learning model to the satellite-based observational datasets to compute DIC concentra-
412 tions at 1° horizontal resolution and at the same vertical levels used in the B-SOSE model. DIC concentrations were
413 computed at a 5-day resolution over the period between 1993 – 2019, for which the input variables were available.
414 Chlorophyll-a concentrations were only available after 1997 and for the prior years, climatologically-averaged chl-a
415 concentrations computed over 1997 – 2019 were used. Same technique was applied to a previous neural network
416 predicting $p\text{CO}_2$ ³. We then divided the obtained DIC concentration data into three decadal time periods: 1993-1999,
417 2000-2009, and 2010-2019. This division was useful in comparing the evolution of linear trends across different sec-
418 tors of the Southern Ocean and relating our results to the previous findings of a weakening trend of the Southern Ocean
419 carbon sink in the 1990s^{10,11} and a strengthening trend in the 2000s^{3,4}.

420 Timeseries over each decadal segment were then extracted at each (latitude,longitude,depth) grid cell. In order to
421 fill in the missing data points in the timeseries, which could result from of ice or cloud cover or other problems with
422 observational data, we used cubic-spline interpolation. However, to prevent over-interpolation at a location where too
423 much data was missing, we applied criteria used in a previous study for gap-filling ocean-carbon data⁶¹. Namely, we
424 restricted the interpolations to locations where data was available (1) for at least five years over each decadal period
425 to ensure that the timeseries was long enough to capture seasonal and long-term trends, and (2) for at least 2/3 of
426 a year at some point in the timeseries in order to extract seasonal cycles. Once the missing data was reasonably
427 filled, we subtracted the seasonal cycle, which we calculated over each time period individually using the statsmodels^f
428 statistical module. Computing seasonal cycle over each decade rather than using a climatological seasonal mean better
429 accounted for any changes in the seasonal cycles over time. Finally, at each grid cell, from the seasonally-detrended
430 data, we computed linear trends over each decadal period using a linear regression model and excluded trends that are
431 not statistically significant (i.e., outside of the 95% confidence level with $p \geq 0.05$). The statistically significant linear
432 trends were then used to produce Fig. 1 and Fig. 2 in the main text.

433 Data Availability

434 Published dataset of DIC concentrations over 1993-2019 period computed by the deep-learning model presented in
435 this study can be found at <https://doi.org/10.5683/SP2/FTQYTV>.

436 Code Availability

437 Codes for Phase 1 and 2 training and testing of the model and for computing DIC from satellite-based products decribed
438 in Methods can be found at https://github.com/tailonghe/Southern_Ocean_Carbon.

^f<https://www.statsmodels.org/>

439 References

- 440 [49] Jürgen Schmidhuber. “Deep learning in neural networks: An overview”. In: *Neural Networks* 61 (Jan. 2015),
441 pp. 85–117. ISSN: 0893-6080. DOI: 10.1016/j.neunet.2014.09.003. URL: [http://dx.doi.org/10.](http://dx.doi.org/10.1016/j.neunet.2014.09.003)
442 [1016/j.neunet.2014.09.003](http://dx.doi.org/10.1016/j.neunet.2014.09.003).
- 443 [50] S.H. Shabbeer Basha et al. “Impact of fully connected layers on performance of convolutional neural networks
444 for image classification”. In: *Neurocomputing* 378 (Feb. 2020), pp. 112–119. ISSN: 0925-2312. DOI: 10.1016/
445 [j.neucom.2019.10.008](http://dx.doi.org/10.1016/j.neucom.2019.10.008). URL: [http://dx.doi.org/10.1016/j.](http://dx.doi.org/10.1016/j.neucom.2019.10.008)
- 446 [51] Sepp Hochreiter and Jürgen Schmidhuber. “Long Short-Term Memory”. In: *Neural Comput.* 9.8 (Nov. 1997),
447 pp. 1735–1780. ISSN: 0899-7667. DOI: 10.1162/neco.1997.9.8.1735. URL: [https://doi.org/10.](https://doi.org/10.1162/neco.1997.9.8.1735)
448 [1162/neco.1997.9.8.1735](https://doi.org/10.1162/neco.1997.9.8.1735).
- 449 [52] Hao Li et al. *Visualizing the Loss Landscape of Neural Nets*. 2018. arXiv: 1712.09913 [cs.LG].
- 450 [53] Diederik P. Kingma and Jimmy Ba. *Adam: A Method for Stochastic Optimization*. 2017. arXiv: 1412.6980
451 [cs.LG].
- 452 [54] Tim DeVries et al. “Decadal trends in the ocean carbon sink”. In: *Proceedings of the National Academy of*
453 *Sciences* 116.24 (2019), pp. 11646–11651.
- 454 [55] Eric D Galbraith et al. “Regional impacts of iron-light colimitation in a global biogeochemical model”. In:
455 *Biogeosciences* 7.3 (2010), pp. 1043–1064.
- 456 [56] Matthew R Mazloff, Patrick Heimbach, and Carl Wunsch. “An eddy-permitting Southern Ocean state estimate”.
457 In: *Journal of Physical Oceanography* 40.5 (2010), pp. 880–899.
- 458 [57] Dorothee CE Bakker et al. “An update to the Surface Ocean CO₂ Atlas (SOCAT version 2)”. In: *Earth System*
459 *Science Data* 6.1 (2014), pp. 69–90.
- 460 [58] Fabrice Bonjean and Gary SE Lagerloef. “Diagnostic model and analysis of the surface currents in the tropical
461 Pacific Ocean”. In: *Journal of Physical Oceanography* 32.10 (2002), pp. 2938–2954.
- 462 [59] H. Hersbach et al. “ERA5 hourly data on pressure levels from 1979 to present”. In: *Copernicus Climate Change*
463 *Service (C3S) Climate Data Store (CDS)* (2018). DOI: 10.24381/cds.bd0915c6.
- 464 [60] Sayaka Yasunaka et al. “Arctic Ocean CO₂ uptake: an improved multiyear estimate of the air–sea CO₂ flux
465 incorporating chlorophyll a concentrations”. In: *Biogeosciences* 15.6 (2018), pp. 1643–1661.
- 466 [61] Steve D Jones et al. “A statistical gap-filling method to interpolate global monthly surface ocean carbon dioxide
467 data”. In: *Journal of Advances in Modeling Earth Systems* 7.4 (2015), pp. 1554–1575.

468 Acknowledgements

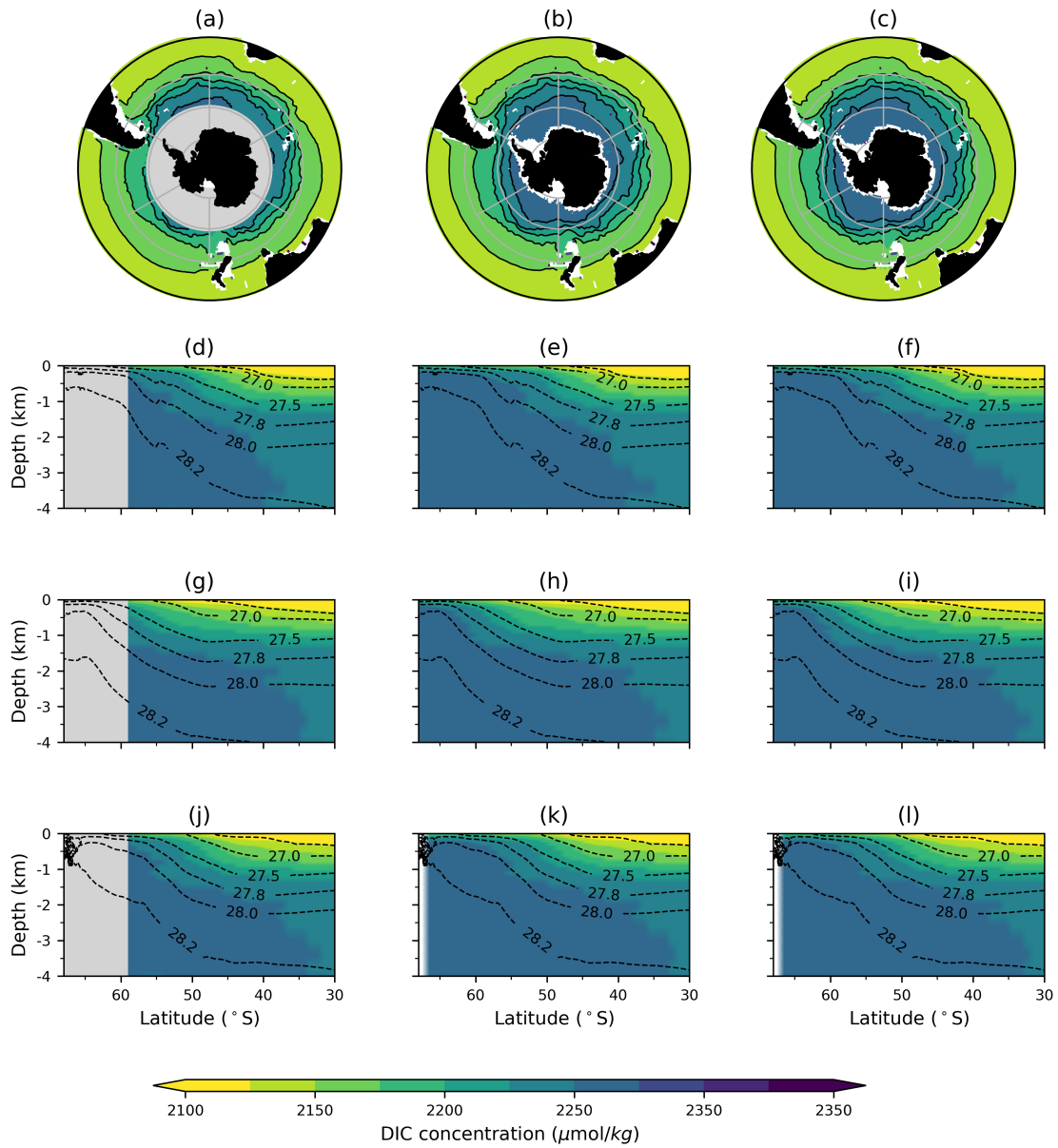
469 We acknowledge the support of the Natural Sciences and Engineering Research Council of Canada (NSERC; Grant
470 No. RGPIN-2015-03684). Data were collected and made freely available by the Southern Ocean Carbon and Cli-
471 mate Observations and Modeling (SOCCOM) Project funded by the National Science Foundation, Division of Polar
472 Programs (NSF PLR -1425989 and OPP-1936222), supplemented by NASA, and by the International Argo Program
473 and the NOAA programs that contribute to it. (<http://www.argo.ucsd.edu>), <http://argo.jcommops.org>). The
474 Argo Program is part of the Global Ocean Observing System. Computational resources for the SOSE were provided
475 by NSF XSEDE resource grant OCE130007. Authors thank research teams from Argo, CMEMS, GLODAP, Glob-
476 Colour, ERA5, NOAA OCADS, OSCAR, and SOCCOM for making the data publicly available. Computations were
477 performed at the SHARCNET HPC Consortium, funded by the Canada Foundation for Innovation under Compute
478 Canada.

479 Author contributions

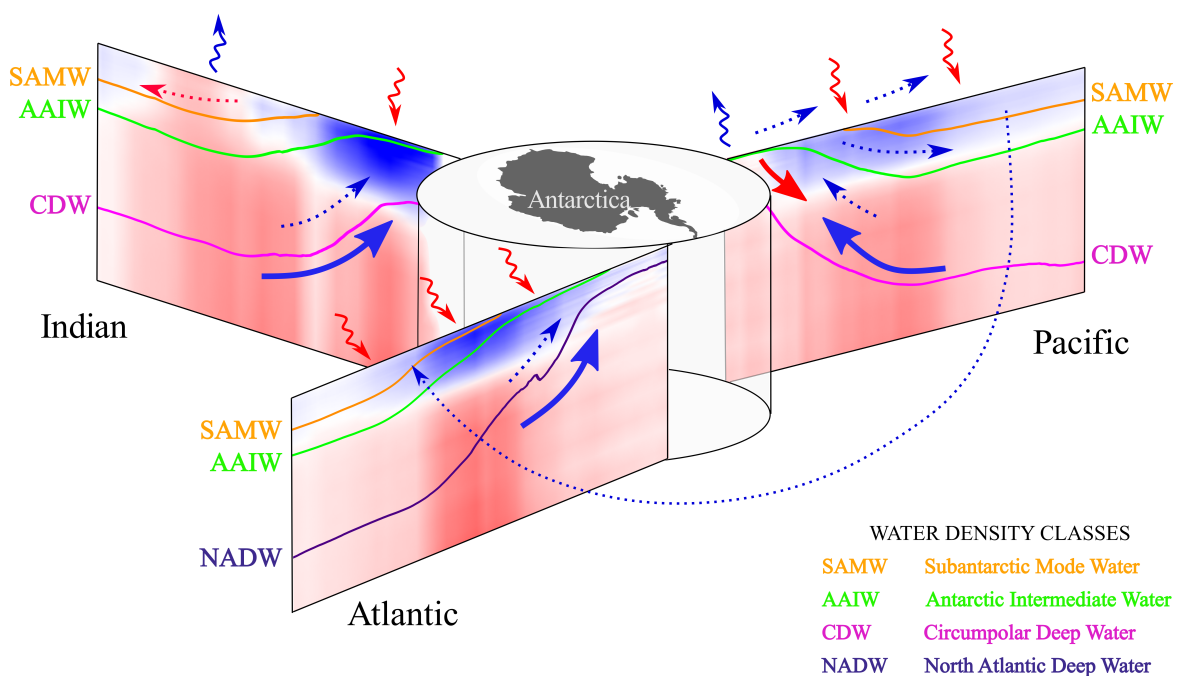
480 V.Z. designed the project and performed linear trend analysis. T.H. and Z.W. developed and trained the deep-learning
481 model under the supervision of V.Z. and N.G. V.Z. wrote the manuscript with input from N.G.

482 Competing interests

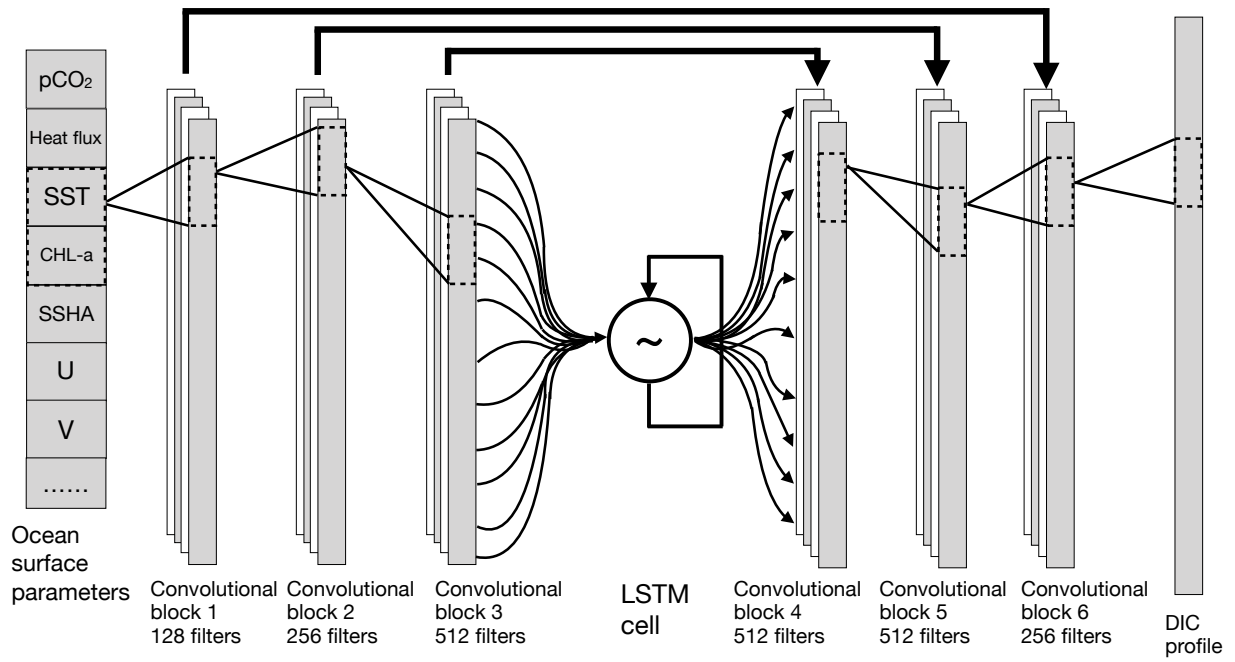
483 Authors report no competing interests.



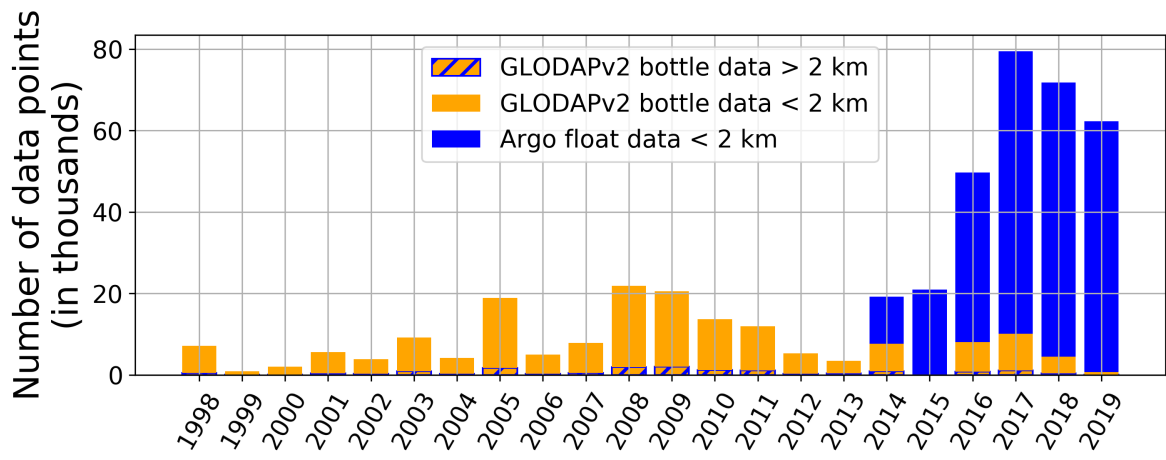
Extended Data Figure 1: **DIC concentrations computed using deep learning model: (left) 1993-1999, (middle) 2000-2009, (right) 2010-2019.** (a-c) Decadal averages of DIC concentrations over top 1 km with contours, zonal means of (d-e) Atlantic, (g-i) Pacific, and (j-l) Indian Oceans. Black dashed contours correspond to isosurfaces of neutral density γ_N from B-SOSE averaged zonally and temporally over 2008-2012 (unlabeled contour: $\gamma_N = 26.6 \text{ kg/m}^3$).



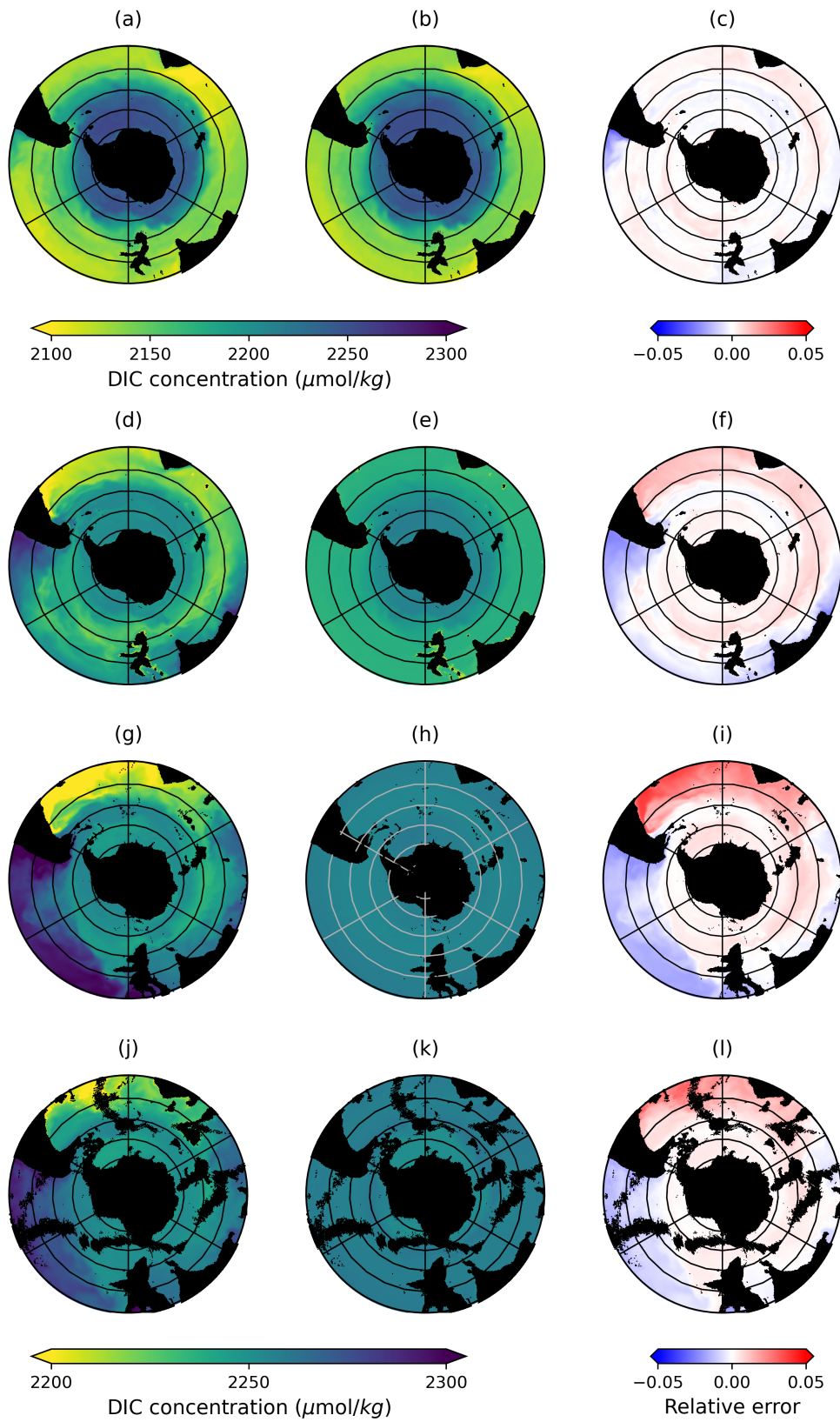
Extended Data Figure 2: **Schematic of the mechanisms affecting DIC trends in the 2000s and 2010s between 30 and 75°S broken down by ocean sectors.** Solid colored lines trace out representative density surfaces of each water-mass (SAMW, AAIW, CDW, NADW). Blue (red) color shading indicates decreasing (increasing) DIC trends over 2000 – 2019. Curly arrows mark buoyancy forcing at the surface: blue (red) indicating buoyancy loss, i.e. input of denser water (buoyancy gain, i.e. input of lighter water). Solid thick arrows mark changes in ocean circulation: blue (red) indicating weakening (strengthening) flow in the indicated direction. Small dotted arrows mark relative strength of DIC transport: blue (red) indicating weakening (strengthening) transport or transport of lower (higher) DIC concentrations.



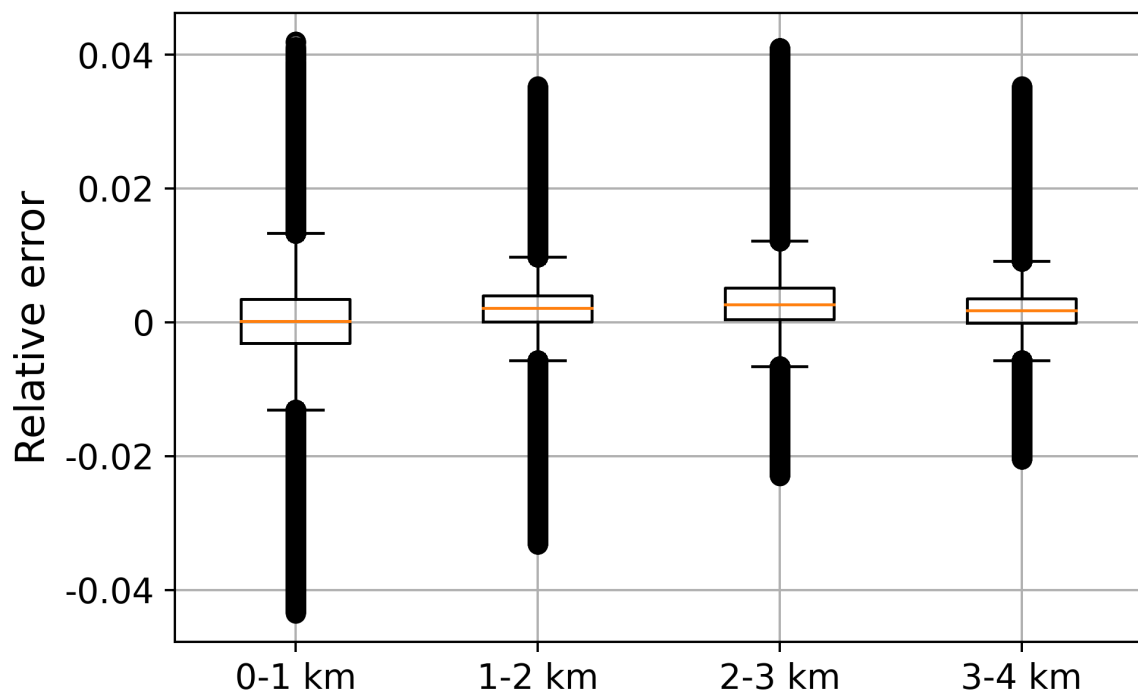
Extended Data Figure 3: **Diagram of the one-dimensional recurrent U-net.** In each convolutional block, input data is fed through 1 fully-connected layer and then filtered by 2 convolutional layers.



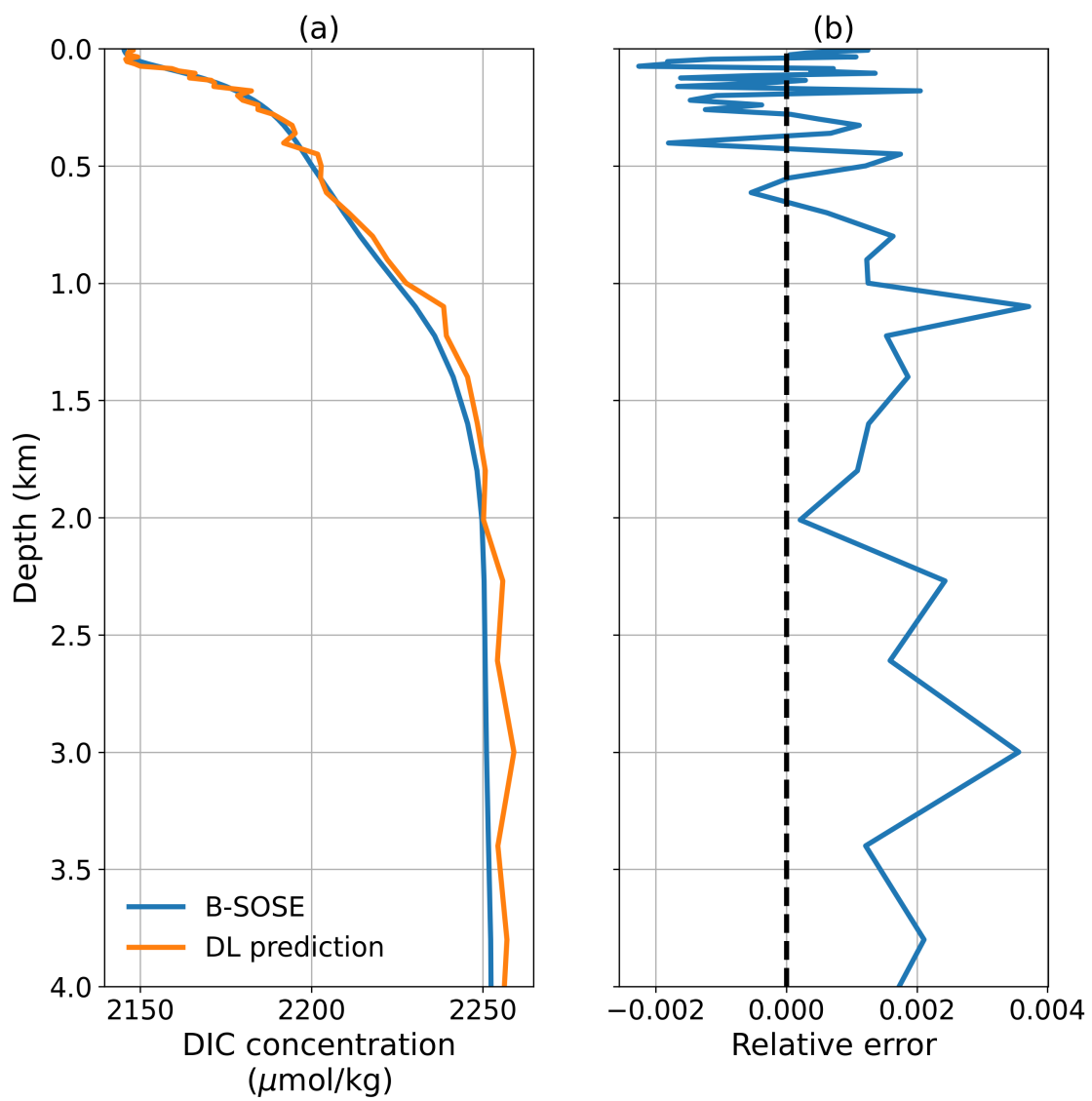
Extended Data Figure 4: **Number of interpolated in situ data points in each year between 1998 and 2019**



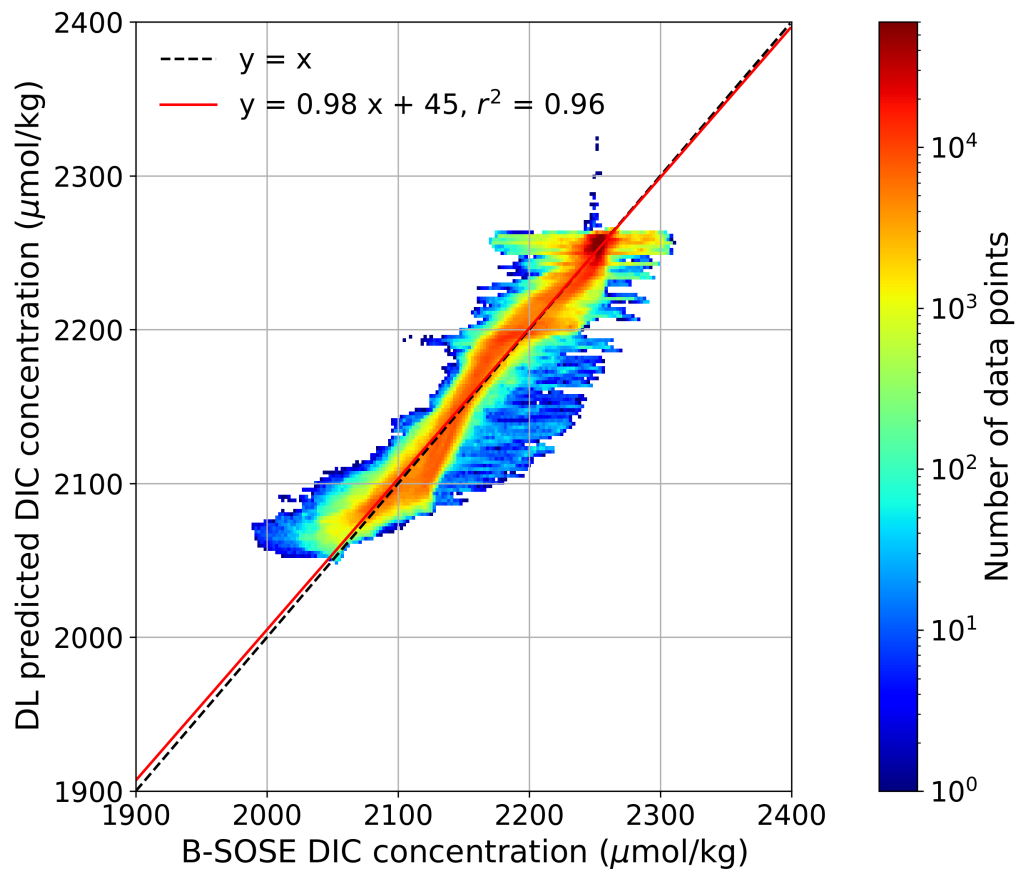
Extended Data Figure 5: **DIC concentration vertically averaged over different depth intervals.** (left) B-SOSE DIC concentration from B-SOSE averaged over, (middle) DIC concentration predicted by the deep learning model, and (right) relative errors of the deep learning model predictions. All variable are averaged over: (a-c) 0-1 km, (d-f) 1-2 km, (g-i) 2-3 km, and (j-l) 3-4 km.



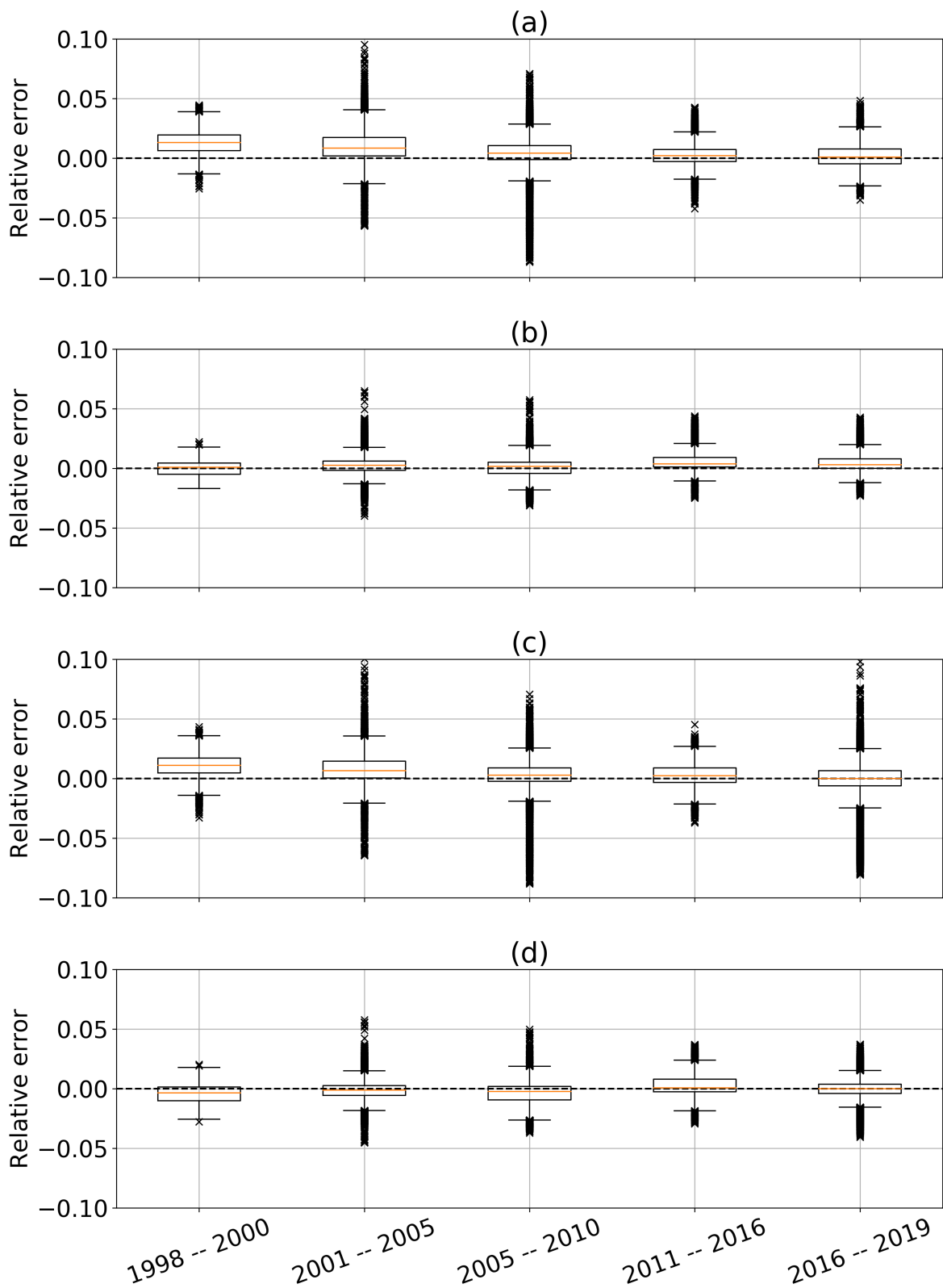
Extended Data Figure 6: **Box-and-whiskers plot of relative errors between deep learning model predictions and B-SOSE DIC concentration over different depth intervals.** Relative errors are calculated at each B-SOSE grid point, averaged over the test period (year 2012). In box-plots, center line: median; box limits: upper and lower quartiles; whiskers: $1.5\times$ interquartile range; points: outliers.



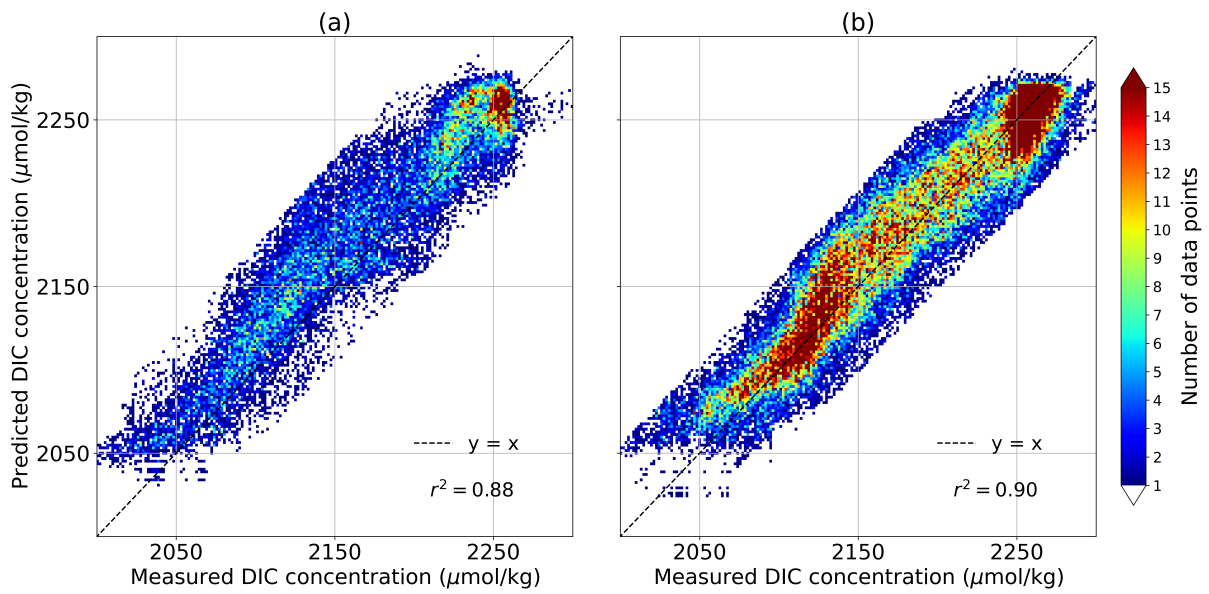
Extended Data Figure 7: **Comparison between B-SOSE and deep learning model predicted DIC profiles, averaged within the test period (year 2012).** (a) DIC concentration with depth, and (b) horizontally-averaged relative errors with depth.



Extended Data Figure 8: **Correlation between B-SOSE and deep learning model predicted DIC concentrations.** DIC concentration at each B-SOSE grid is temporally averaged over the test period (year 2012). Red lines show the linear fit with r^2 value reported in the legend compared with one-to-one line in dotted black.



Extended Data Figure 9: **Box-and-whiskers plot of relative errors for the predicted DIC concentrations compared to the measured DIC.** (a-b) For model trained using GLODAP bottle data only, and (c-d) model trained using both GLODAP bottle data and SOCCOM Argo float data. (a,c) errors between 0-2 km, and (b,d) errors between 2-4 km. In box-plots, center line: median; box limits: upper and lower quartiles; whiskers: $1.5\times$ interquartile range; crosses: outliers.



Extended Data Figure 10: **Correlation between DIC predicted by the deep learning model and measured DIC.** (a) using GLODAP bottle data only, and (b) using bottle data and SOCCOM Argo float data. One-to-one line is plotted in dotted black along with the regression coefficient r^2 .